

A Model for the Stray Light Contamination of the UVCS Instrument on SOHO

S. R. Cranmer¹ · L. D. Gardner¹ · J. L. Kohl¹

© Springer 2010

Abstract We present a detailed model of stray-light suppression in the spectrometer channels of the *Ultraviolet Coronagraph Spectrometer* (UVCS) on the SOHO spacecraft. The control of diffracted and scattered stray light from the bright solar disk is one of the most important tasks of a coronagraph. We compute the fractions of light that diffract past the UVCS external occulter and non-specularly pass into the spectrometer slit. The diffracted component of the stray light depends on the finite aperture of the primary mirror and on its figure. The amount of non-specular scattering depends mainly on the micro-roughness of the mirror. For reasonable choices of these quantities, the modeled stray-light fraction agrees well with measurements of stray light made both in the laboratory and during the UVCS mission. The models were constructed for the bright H I Ly α emission line, but they are applicable to other spectral lines as well.

Keywords: Instrumental Effects; Spectrum, Ultraviolet

1. Introduction

Until the 20th century, total solar eclipses were the only means of observing the hot solar corona. However, with the invention of the internally-occulted coronagraph by Bernard Lyot in the 1930s (Billings, 1966; Koutchmy, 1988), the addition of an external occulter (Evans, 1948; Newkirk and Bohlin, 1963), and the development of an ultraviolet coronagraph spectrometer in the 1970s (Kohl *et al.*, 1978; Kohl *et al.*, 1980), a continuous and detailed exploration of coronal plasma physics became possible. Such instruments, combined with spectroscopic diagnostic techniques, have become powerful tools for measuring a wide range of plasma properties in the acceleration regions of solar wind streams and coronal mass ejections (see, *e.g.*, Newkirk, 1967; Withbroe *et al.*, 1982; Kohl *et al.*, 2006; Howard *et al.*, 2008; Cranmer, 2009).

One of the most demanding requirements of a successful coronagraph is the suppression of “stray light” scattered from the bright solar disk. The coronal emission tends to be many orders of magnitude less bright than the emission from the Sun’s lower atmospheric layers. At a heliocentric distance of two solar radii (R_{\odot}), the extended

¹ Harvard-Smithsonian Center for Astrophysics, 60 Garden Street,
Cambridge, MA 02138, USA
email: scanmer@cfa.harvard.edu, jkohl@cfa.harvard.edu,
lgardner@cfa.harvard.edu

corona is approximately 10^{-8} times less bright than the disk at visible wavelengths. In the ultraviolet the corona is relatively brighter, but still is only about 10^{-6} (at H I Ly α 1216 Å) to 5×10^{-6} (at Mg x 610 Å) times the disk intensity. These numbers correspond to the lowest-intensity regions off the solar limb (coronal holes). Because light rays coming from the disk are separated in angle by only fractions of a degree from the rays coming from the corona, there are many ways that a small fraction of the former can easily contaminate the latter. A key purpose of an efficient coronagraph is to suppress as much of this stray light as possible through the use of re-imaging, occulters, baffles, light traps, and also by making the mirrors as smooth and accurate as possible.

This paper presents a detailed analysis of the stray light properties of the *Ultraviolet Coronagraph Spectrometer* (UVCS) instrument (Kohl *et al.*, 1995; Kohl *et al.*, 1997) onboard the *Solar and Heliospheric Observatory* (SOHO) spacecraft (Domingo *et al.*, 1995; Fleck and Švestka, 1997). At present, there are only a few published measurements of the stray light properties of UVCS, and many observations have been taken without dedicated stray-light measurements. Thus, there is a need for a model that predicts the stray-light intensities at ultraviolet wavelengths. The dominant source of UVCS stray light has been shown to be diffracted light from the external occulter that is non-specularly scattered by the telescope mirror into the spectrometer entrance slits. Kohl *et al.* (1995) described other possible contributions to the stray light and explained how they are controlled. This paper primarily describes the non-specular scattering from the telescope mirror, which accounts for essentially all of the UVCS stray light background.

The model developed for this paper applies mainly to the Ly α spectrometer channel of UVCS, which observes the strong H I Ly α 1216 Å emission line and other spectral lines within a wavelength range of 1100 – 1361 Å. The model also is valid for the O VI channel, which is optimized to observe the O VI 1032, 1037 Å doublet, as well as other spectral lines within a wavelength range of 937 – 1126 Å in first order. The redundant Ly α path of this channel can be used to observe from 1166 to 1272 Å in first order as well. The stray-light properties of the UVCS white-light channel (WLC) were described by Romoli *et al.* (1993) and are not discussed here.

The outline of this paper is as follows. Section 2 presents an overview of the relevant UVCS optical paths and occulting surfaces. Section 3 describes how much light from the solar disk is diffracted by the UVCS external occulter, and Section 4 describes how much of this light enters the spectrometer slit via finite-aperture diffraction and non-specular scattering. Section 5 summarizes how the contributions from a range of locations on the UVCS primary mirror are summed to determine the total stray light intensity. Section 6 presents the results of a calculation for H I Ly α stray light as a function of the observation height and compares the model predictions with measurements. Section 7 contains a brief summary of the paper and a discussion of the capabilities of future instrumentation. Finally, the Appendix describes how the theoretical rates of non-specular scattering were derived separately for the effects of mirror micro-roughness and finite-aperture diffraction.

2. UVCS Optical Path Geometry

The UVCS instrument contains three reflecting telescopes that feed two ultraviolet toric-grating spectrometers and one white-light polarimeter (Kohl *et al.*, 1995). Unlike

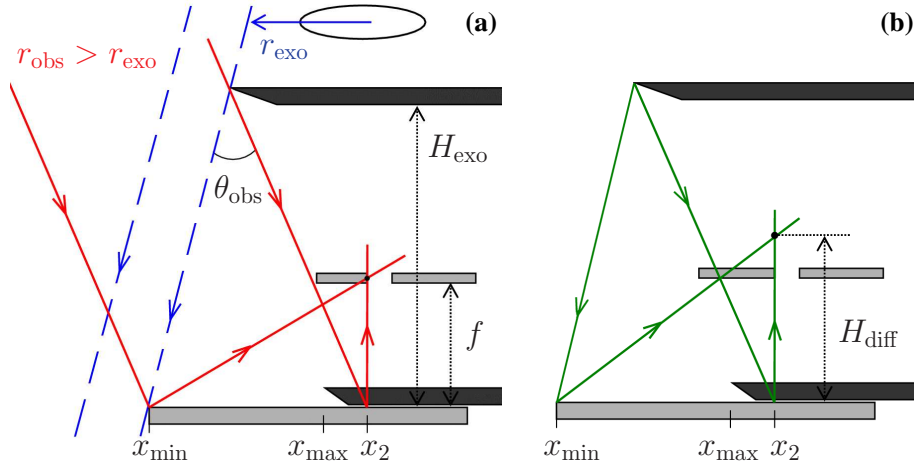


Figure 1. (a) Schematic illustration of the UVCS/SOHO optical path for coronal rays (*i.e.*, light coming from an infinite distance). (b) Optical paths for rays diffracted from the tip of the external occulter. The horizontal distance along the mirror [x] increases from left to right. In both panels, the mirror is the light-gray surface at the bottom, the external occulter is the dark-gray surface at the top (at a distance H_{exo} above the mirror), and the spectrometer slit is the light-gray split surface at a distance f above the mirror. The internal occulter is the dark-gray surface sitting on top of the mirror and covering up all $x > x_{\text{max}}$.

many other coronagraphs, the UVCS occulting surfaces are linear, not circular, so that the incoming rays are well matched to the linear geometry of the spectrometer entrance slit. Rays from the bright solar disk are blocked by an external occulter and enter a sunlight trap, whereas rays from the extended corona are reflected by the primary mirror into the spectrometer slits. These slits are oriented in the direction tangent to the solar limb. The coronal images can be positioned on the slit centers in heliocentric radius [r] anywhere between about 1.4 and $10 R_{\odot}$ and rotated around the Sun in position angle. The slit length projected on the sky is 40 arcminutes, or approximately $2.5 R_{\odot}$ in the corona, and the slit width can be adjusted to optimize the desired spectral resolution and count rate.

Figure 1a illustrates the geometry for light coming from the extended corona, being reflected by the UVCS primary mirror, and entering the spectrometer slit. The geometry is the same for the Ly α and O VI channels. This diagram is not intended to be an accurate schematic of the instrument, however. We illustrate the mirror as being flat, but we take account of the fact that it focuses coronal light on the slit. The spatial scales are exaggerated in order to show how the relevant angles and distances are defined below. For example, all angles of reflection and scattering are small (*i.e.*, near normal incidence on the mirror), with $\sin \theta \approx \tan \theta \approx \theta$ applying in most cases. Because the analysis of this paper is mainly concerned with relative *departures* from the specularly reflected ray paths, it is unimportant which of the rays in Figure 1 is portrayed as exactly normal to the mirror.

The external occulter is shown as the upper-most horizontal surface in Figure 1. It is positioned so that all specular rays from heliocentric distances less than a given distance r_{exo} miss the mirror entirely and are absorbed in the UVCS sunlight trap (see dashed blue rays). Thus, we can only observe the extended corona at radii $r_{\text{obs}} > r_{\text{exo}}$ (see solid red rays). For UVCS, $r_{\text{exo}} = 1.2 R_{\odot}$. In Figure 1, the horizontal coordinate x is

measured along the length of the mirror. The origin $x = 0$ is defined as the left edge where the ray coming from r_{exo} that just barely misses the external occulter also just barely misses the mirror.

The observation angle θ_{obs} , which corresponds to the angular distance between the desired observation height and the rays that just miss the mirror, is given by

$$\theta_{\text{obs}} = \theta_{\odot} \left(\frac{r_{\text{obs}} - r_{\text{exo}}}{R_{\odot}} \right) \quad (1)$$

where θ_{\odot} is the angle subtended by one solar radius on the sky. For the mean heliocentric distance of the SOHO spacecraft, $\theta_{\odot} = 4.698 \times 10^{-3}$ radians = $0.269^{\circ} = 968.9''$. For UVCS, the external occulter is positioned at a height of $H_{\text{exo}} = 170$ cm above the mirror. The maximum possible region of the mirror that can be illuminated by the corona extends from $x = 0$ to $x = H_{\text{exo}} \tan \theta_{\text{obs}}$. We can define these two limiting positions as x_1 and x_2 , respectively. The area of the mirror exposed to coronal light can be reduced by moving the UVCS internal occulter (which sits on top of the mirror) to the left of its default position by a distance x_{int} . The default (“zero over-occluding”) position corresponds exactly to x_2 , and most UVCS observations have been made with the internal occulter positioned at $x_{\text{int}} = 1.5$ mm to the left of x_2 . Thus, the so-called “vignetting function” of UVCS is defined by the radially increasing mirror area that is filled by coronal rays. For a given observation height, the unvignetted mirror area spans the distances between $x_{\text{min}} = x_1 = 0$ and $x_{\text{max}} = x_2 - x_{\text{int}}$.

It should also be noted that neither x_2 nor x_{max} can exceed the actual physical size of the mirror in the x -direction, which for UVCS is 7.2 cm. The corresponding maximum observation height at which the mirror is “filled” is $r_{\text{obs}} = 10.3 R_{\odot}$.

Parallel rays from an infinite distance are reflected by the mirror and are focused at the slit, which is positioned at $f = 75$ cm above the mirror. For the orientation shown in Figure 1a, the left edge of the slit is fixed in place (exactly at the focus point) and the right edge of the slit is the part that opens and closes to achieve a given slit width w . In this analysis, all coronal rays – from the coronal region of interest – that are reflected from mirror positions between x_{min} and x_{max} are assumed to pass through the slit.

Figure 1b shows the behavior of light that is *diffracted* from the edge of the external occulter. From the point of view of geometrical optics, these rays all appear to originate approximately at the tip of the external occulter itself (*i.e.*, at a finite distance away from the mirror). Thus, these rays are not focused to a point at f , but instead are focused at a distance H_{diff} above the mirror, which is given by

$$\frac{1}{H_{\text{diff}}} = \frac{1}{f} - \frac{1}{H_{\text{exo}}} \quad (2)$$

and $H_{\text{diff}} = 134.21$ cm for UVCS. Note that the specular rays in Figure 1b are nearly all blocked from entering the slit. The only exception would be the right-most rays that strike the mirror at $x_2 = H_{\text{exo}} \tan \theta_{\text{obs}}$. These are eliminated by just a small amount of over-occluding by the internal occulter. However, the diffracted beams also have substantial energy at non-specular angles, and these are discussed further in Section 4.

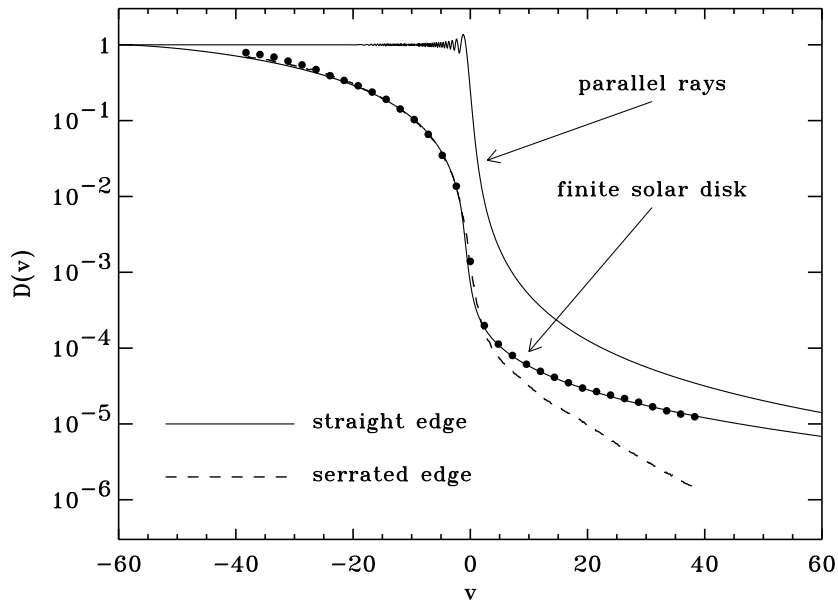


Figure 2. Fractional reduction in irradiance due to diffraction at the external occulter, shown as a function of dimensionless distance [v] behind the occulter. Laboratory measurements for a straight edge (points) and a serrated edge (dashed curve) are compared with computed diffraction curves (solid curves).

3. Diffraction from the External Occulter

The external occulter is the first line of defense against stray-light contamination. In this section, we compute how much light is diffracted by the external occulter and falls onto the mirror. We ignore the diffracted light that does not hit the mirror, but instead strikes other structural components of the instrument where it can undergo multiple reflections before possibly finding its way to the entrance slit. Specifically, we ignore the stray light produced by scattering off the mirror edge and the surface of the internal occulter. These effects can be important at visible wavelengths, but they have been shown to be negligible in the ultraviolet for externally-occulted designs like UVCS (see, *e.g.*, Romoli *et al.*, 1993; Kohl *et al.*, 1995).

The problem of parallel rays diffracting around an ideal one-dimensional straight edge (*i.e.*, a semi-infinite screen) is treated in standard textbooks (*e.g.*, Born and Wolf, 1999; Hecht, 2002). In practice, it has been found that serrated, or “toothed” edges perform better than ideal straight edges (Newkirk and Bohlin, 1963; Koutchmy and Belmahdi, 1987; Verroi *et al.*, 2008). In the late 1980s, laboratory measurements were made at the Smithsonian Astrophysical Observatory for both straight-edged and serrated occulters, in combination with the *Spartan 201* UV coronagraph spectrometer (see Romoli *et al.*, 1993). The laboratory measurements were done with a light source that subtends the same solid angle as the solar disk. The serrated occulter used on UVCS has symmetric sawtooth-shaped notches (*i.e.*, resembling a repeating triangle waveform) with a separation of the peaks, parallel to the occulter edge, of $229 \mu\text{m}$. The depth of the peaks, perpendicular to the occulter edge, is $267 \mu\text{m}$.

Figure 2 illustrates laboratory measurements and theoretical predictions for the reduction in irradiance (*i.e.*, radiative flux) seen as an observer moves progressively into the occulter’s shadow. This quantity is shown specifically for the H I Ly α wavelength, and the distance behind the occulter was converted into dimensionless Fresnel diffraction coordinates

$$v = (x - x_{\odot}) \sqrt{\frac{2}{\lambda H_{\text{exo}}}} \quad (3)$$

where λ is the wavelength of interest and x_{\odot} is the mirror position that corresponds to rays from the near edge of the solar disk that barely miss the external occulter. Because these rays do not strike the mirror, x_{\odot} is negative in our coordinate system, and it is given by $-H_{\text{exo}} \tan(\theta_{\odot}[r_{\text{exo}}/R_{\odot} - 1])$. Thus, all values of v that are relevant for UVCS are positive. We denote the relative irradiance quantity plotted in Figure 2 as $D(v)$.

The uppermost curve in Figure 2 corresponds to parallel rays (*i.e.*, from a point-source on the sky at infinite distance). This is given by

$$D(v) = \frac{1}{2} \left\{ \left[\frac{1}{2} - C(v) \right]^2 + \left[\frac{1}{2} - S(v) \right]^2 \right\} \quad (4)$$

where $C(v)$ and $S(v)$ are the standard Fresnel integrals (Abramowitz and Stegun, 1972). When observing the Sun, this function must be convolved with the finite size of the solar disk on the sky, since the total diffracted light is a combination of beams between the “near edge” of the solar disk (*i.e.*, only $0.2 R_{\odot}$ behind the r_{exo} ray that just grazes the left edge of the mirror) and the “far edge” (up to $2.2 R_{\odot}$ behind the grazing ray). For the H I Ly α emission line, we consider the solar disk to be uniformly bright (Curdt *et al.*, 2008). The result of this numerical convolution (lower solid curve) agrees very well with the measured data for a straight-edge occulter (points) taken with a light source with the same finite solid angle as the Sun (see also Romoli *et al.*, 1993).

It can also be seen from Figure 2 that the serrated edge produced a significantly lower amount of diffraction than the straight edge. The dashed curve corresponding to the serrated edge is denoted $D_s(v)$. The laboratory measurements extended up to an occulting distance corresponding to $v \approx 38$. UVCS observations made at $r_{\text{obs}} \leq 2.74 R_{\odot}$ fall into the range of heights where the laboratory measurements can be applied via interpolation. However, UVCS observations at larger heights require some degree of extrapolation beyond the measured range. For example, the largest height of $r_{\text{obs}} \approx 10 R_{\odot}$ fills the mirror with a range of v values between about 5 and 220. After some experimentation, we found that a power-law extrapolation curve that scales as v^{-3} best reproduced and continued the slope of the measured data. Romoli *et al.* (1993) used an exponential function which may become lower than the v^{-3} curve at large values of v . Thus, our power-law extrapolation may give rise to a slight (but conservative) overestimate of the diffraction at large observation heights.

4. Non-specular Rays Entering the Slit

Each point on the mirror between x_{min} and x_{max} acts as a “source” of solar-disk light that has been diffracted by the external occulter. These specular rays are focused at a

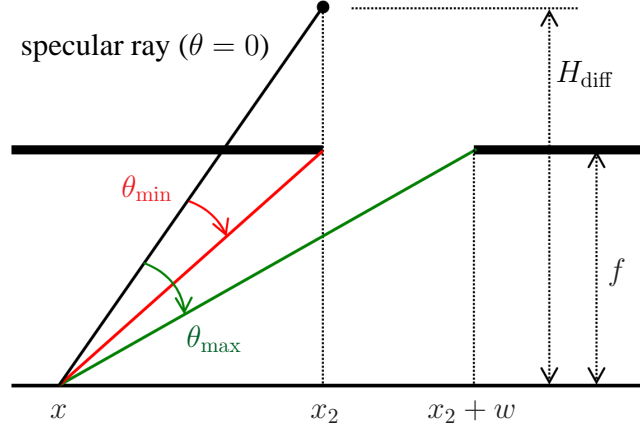


Figure 3. Non-specular geometry for diffracted rays originating at an arbitrary point $[x]$ on the mirror surface and passing through the spectrometer slit.

point H_{diff} above the mirror, and are blocked by the left-side slit edge. However, the light is not concentrated all along the ideal specular ray, but instead has a characteristic *non-specular* spread that subtends a broader range of solid angle. Thus, there are always non-specular rays from the mirror that are able to pass through the slit. Figure 3 illustrates those rays, which are denoted by non-specular angles ranging between θ_{min} and θ_{max} . For a given point $[x]$, the values of these angles are given by

$$\theta_{\text{min}} = \tan^{-1}\left(\frac{H_{\text{diff}}}{x_2 - x}\right) - \tan^{-1}\left(\frac{f}{x_2 - x}\right) \quad (5)$$

$$\theta_{\text{max}} = \tan^{-1}\left(\frac{H_{\text{diff}}}{x_2 - x}\right) - \tan^{-1}\left(\frac{f}{x_2 + w - x}\right) \quad (6)$$

where w is the slit width. Note that for the special case of $x = x_2$, some specular rays pass through the slit since $\theta_{\text{min}} = 0$ and $\theta_{\text{max}} = \tan^{-1}(w/f)$. Of course, for any finite amount of internal over-occluding, these rays never get reflected at all, since we endeavor to keep all rays that reach the mirror at $x < x_{\text{max}} < x_2$.

The fraction of reflected light that passes non-specularly into the spectrometer slit is computed by summing the effects of two distinct physical processes: *i*) diffraction due to the finite size of the mirror, and *ii*) scattering due to mirror micro-roughness. The Appendix gives a derivation of these two components. We note that this separation into two parts is an approximation of the full angular distribution of non-specular intensity, which for UVCS is not known with sufficient detail to specify as a single function. It is useful to specify these two effects separately so that different assumptions about their origin and magnitude can be made without each “contaminating” the other. Taking their direct sum may result in an amount of non-specular scattering that is slightly larger than the actual combined effect of these two processes, but this errs on the side of making a conservative overestimate of the stray light. The combined differential scattering and

diffraction can thus be expressed as

$$\frac{dI}{I_0 d\theta_x} = \frac{\lambda}{2\pi^2 D_x \theta_x^2} \left[W + \frac{D_x}{\Lambda} \left(\frac{32\pi^3 \sigma^2}{\lambda^2} \right) \right], \quad (7)$$

where $D_x = x_{\max} - x_{\min}$ is the illuminated mirror width, θ_x is the non-specular angle measured in the plane of Figure 3, W is a wing enhancement factor that takes account of deviations from a perfect diffraction aperture, σ is the root-mean-squared (r.m.s.) micro-roughness of the mirror, and Λ is a horizontal coherence length for the mirror's non-ideal surface modulations. The first term in square brackets above takes account of diffraction due to the mirror's finite size, and the second term accounts for micro-roughness.

Equation (7) assumes both that the micro-roughness is small compared to the wavelength (*i.e.*, $\sigma \ll \lambda$) and that the non-specular angles are large compared to the angular size of the specular beam (*i.e.*, $\theta_x \gg \lambda/D_x$). We denote the relative fraction of the diffracted solar-disk light on the mirror surface that makes it through the slit as dI/I_0 . This fraction is given by integrating over all non-specular angles between θ_{\min} and θ_{\max} , and

$$\frac{dI}{I_0} = \int_{\theta_{\min}}^{\theta_{\max}} d\theta_x \frac{dI}{I_0 d\theta_x}. \quad (8)$$

Note that the integration over the other non-specular angle θ_y is discussed in the Appendix.

5. Flux Normalization

Next, it is necessary to compute the total flux that comes from a given location on the mirror and passes through a given part of the slit. We must take account of the full two-dimensional shape of the slit aperture; *i.e.*, not just the width [w] but also the height [h] of the spatial element of interest (in the direction normal to the page in Figure 1). From the point of view of the mirror, the solid angle of the slit is given by $\Omega_{\text{slit}} = wh/f^2$. The flux of light from the extended corona is thus given by

$$F_{\text{cor}}(x) = \begin{cases} I_{\text{cor}} \Omega_{\text{slit}}, & x_{\min} < x < x_{\max} \\ 0 & \text{otherwise} \end{cases} \quad (9)$$

where I_{cor} is the coronal intensity, in units of $\text{erg s}^{-1} \text{cm}^{-2} \text{sr}^{-1}$ (*i.e.*, integrated across the spectral line). We assume that I_{cor} is constant over the slit aperture.

The stray light, which began its life as the direct solar-disk intensity I_{\odot} , is attenuated by diffraction and non-specular scattering. Without this attenuation, the flux from the solar disk is given by $I_{\odot} \Omega_{\odot}$, where Ω_{\odot} is the solid angle of the Sun in the sky (essentially $\pi\theta_{\odot}^2$). However, because of the finite slit height h , only a fraction of this flux would make it through the slit. In the limiting case where the angle subtended by the slit-height direction (approximately h/f) is small compared to the solar diameter ($\delta_{\odot} = 2\theta_{\odot}$), the piece of the solar disk that is “seen” through the slit is only a strip with solid angle $\Omega_{\text{strip}} \approx h\delta_{\odot}/f$. In the opposite limit of $h/f \geq \delta_{\odot}$, then $\Omega_{\text{strip}} = \Omega_{\odot}$. The

code used to compute the stray light uses an exact expression that bridges these limiting cases, which for $h/f \leq \delta_{\odot}$ is given by

$$\Omega_{\text{strip}} = \frac{\delta_{\odot}^2}{2} \tan^{-1} \left(\frac{h}{\sqrt{\delta_{\odot}^2 f^2 - h^2}} \right) + \frac{h \sqrt{\delta_{\odot}^2 f^2 - h^2}}{2f^2}. \quad (10)$$

For all of the numerical calculations shown below, however, the approximation $\Omega_{\text{strip}} \approx h\delta_{\odot}/f$ is reasonably valid. Thus, the fully attenuated stray-light flux is

$$F_{\text{stray}}(x) = I_{\odot} \Omega_{\text{strip}} D_s(v) \frac{dI}{I_0}. \quad (11)$$

The two fluxes defined above represent power per unit mirror surface area. The total power, in erg s^{-1} , that passes through the slit for the two cases is given by integrating over the mirror surface:

$$P_{\text{cor}} = \int \int dx dy F_{\text{cor}}(x) \quad (12)$$

$$P_{\text{stray}} = \int \int dx dy F_{\text{stray}}(x) \quad (13)$$

where the integration over the y -coordinate (the mirror dimension out of the page in Figure 1) is trivial because the fluxes are independent of y . The x -coordinate ranges from x_{min} to x_{max} . The y -coordinate ranges from $y_{\text{min}} = 0$ to $y_{\text{max}} = 5$ cm (the latter being the UVCS mirror height).

Finally, the ‘‘calibrated’’ measurement for stray-light intensity can be constructed. Once the total power quantities defined above are known, the corresponding intensities can be computed simply by dividing either P_{cor} or P_{stray} by the product $A\Omega_{\text{slit}}$. The illuminated mirror area is given by

$$A = (y_{\text{max}} - y_{\text{min}})(x_{\text{max}} - x_{\text{min}}). \quad (14)$$

This process is unnecessary for the coronal intensity, since I_{cor} was used in its initial definition [Equation (9)]. However, the stray-light intensity [I_{stray}] is computed in this way by dividing P_{stray} by $A\Omega_{\text{slit}}$ directly. We do not consider any instrumental properties beyond the entrance slit (*e.g.*, efficiencies of the grating and detector) because they do not distinguish between coronal and stray light.

6. Results

We implemented the above constraints on ray geometry, external-occulter diffraction, non-specular scattering, and flux calibration into an IDL code that predicts the stray-light intensity [I_{stray}] for various configurations of the UVCS instrument. A standard set of models for the H I Ly α spectral line was constructed with the geometric parameters given in the previous sections, as well as the following choices for the internal occulter position ($x_{\text{int}} = 1.5$ mm), slit width ($w = 100$ μm), and the angular resolution

of the spatial element of interest along the slit (10 arcseconds, or $h = 36.4 \mu\text{m}$ on the slit).

In the models presented here, the two main properties of the mirror that describe its diffraction and non-specular scattering are the r.m.s. micro-roughness [σ] and the r.m.s. wavefront error [ω]. As described in the Appendix, the wavefront error is a single parameter that characterizes the large-scale figure error of the mirror. This parameter determines the angular width of the specular beam and the enhancement of the large-angle diffraction wing. The figure error can also be expressed as an effective mirror size D_{eff} , which acts as a large-scale coherence length analogous to the micro-roughness coherence length [Λ]. Although no precise measurements of these quantities exist for the UVCS mirrors, there are several reasonable lower and upper bounds that can be applied.

First, a “best-case” model can be constructed with the assumption of zero micro-roughness. For $\sigma = 0$, the non-specular rays are solely the result of diffraction around the finite aperture of the primary mirror. The lowest possible level of non-specular intensity is consistent with the diffraction-limited case of no figure error ($\omega = 0$). This limit is interesting because it provides a true lower bound on the stray light that cannot be improved upon without changing the instrument design.

Second, we constructed a model with empirical upper limits on the micro-roughness and figure error. Scattering measurements were made with a helium-neon laser on the mirror eventually chosen for flight as the Ly α channel primary (Leviton *et al.*, 1998). These measurements were consistent with a value for the r.m.s. micro-roughness of approximately 20 Å. We note that this determination is dependent on a particular numerical model for the scattering properties of mirrors, which has been described by Saha *et al.* (1996). Nonetheless, we use $\sigma \approx 20 \text{ \AA}$ as an approximate upper limit for the UVCS primary mirrors. Two independent determinations of the spatial coherence lengths of the mirror were found that agree with one another reasonably well:

- i) We used the Leviton *et al.* (1998) measurements of non-specular scattering to put a limit on the mirror’s coherence length. The large-angle limit of Equation (26) can be used to show that

$$\Lambda \approx \frac{8\pi\sigma^2}{\lambda\theta^3} \left(\frac{dI}{I_0 d\Omega} \right)^{-1}. \quad (15)$$

Measurements of $dI/I_0 d\Omega$ were taken at angles [θ] corresponding to heliocentric distances between 0.95 and 11.3 R_{\odot} . The mean value of Λ for all of these measurements, derived from Equation (15), was found to be 1.36 cm. This results in a ratio [D_x/Λ] = 5.3 for the full unvignetted mirror width $D_x = 7.2 \text{ cm}$.

- ii) Another determination of the mirror’s performance can be found from the measured UVCS spatial resolution. The most definitive upper limits on spatial resolution were obtained from in-flight observations of the star $\rho \text{ Leo}$, made in August 1996. For H I Ly α , the measured full-width at half-maximum (FWHM) of the spatial resolution element was found to be 5.7 arcseconds. Although some fraction of this value may be attributable to other instrumental factors, it is useful to assign it all to the mirror’s figure error to obtain an upper limit. Ideally, the FWHM should be converted into an angular half-width [θ_s] as defined in the Appendix. If the measured profile were a Gaussian beam, it would encompass 83.8% of the encircled intensity out to an

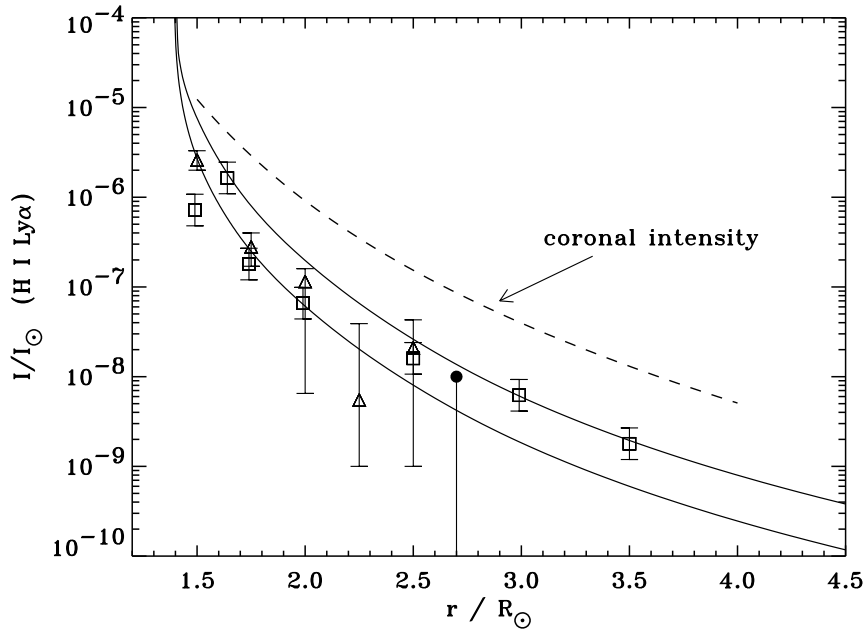


Figure 4. Comparison of modeled and observed stray-light suppression ratios $I_{\text{stray}}/I_{\odot}$. Models are shown for the lower-limit case of no micro-roughness and diffraction-limited optics (lower solid curve) and an empirical upper limit on the mirror parameters (upper solid curve). The stray-light measurements (points) are described in the text. For comparison, the H I Ly α intensity measured by UVCS in a polar coronal hole is also shown (dashed curve).

angular half-width of about 0.8 times the FWHM. Because this is so close to unity, and because its exact shape is unknown, we just use the FWHM itself to assume an upper-limit value of $\theta_s \approx 5.7$ arcseconds. Thus, Equation (32) gives $D_{\text{eff}} \approx 0.54$ cm. The stellar observations were taken at a heliocentric distance $r_{\text{obs}} \approx 5.2 R_{\odot}$ at which the unvignetted mirror width was $D_x \approx 3.03$ cm. The derived ratio D_x/D_{eff} was found to be 5.6.

Because the ratios D_x/Λ and D_x/D_{eff} were found to be in good agreement with one another, we make the tentative assumption that one can treat Λ and D_{eff} roughly interchangeably for this analysis. Thus, we adopt a mean ratio $D_x/\Lambda = 5.45$ and we use Figure 5 to give the corresponding wavefront error $\omega/\lambda \approx 0.23$ and wing enhancement ratio $W \approx 1.78$.

Figure 4 shows the numerically computed $I_{\text{stray}}/I_{\odot}$ ratios that correspond to the two limiting sets of parameters described above. The lower-limit set of mirror parameters ($\sigma = 0$, $D_x/\Lambda = 1$) shows the effect of having only diffraction contribute to the stray light. For the empirical upper-limit parameters ($\sigma = 20 \text{ \AA}$, $D_x/\Lambda = 5.45$) the micro-roughness contributed roughly half (45%) of the total stray light. The following parameterized fits were found to be good representations of the model curves in Figure 4,

$$\left(\frac{I_{\text{stray}}}{I_{\odot}}\right)_{\text{lower}} = \frac{3.14 \times 10^{-8}}{([r/R_{\odot}] - 1.121)^{4.56}}, \quad (16)$$

$$\left(\frac{I_{\text{stray}}}{I_{\odot}}\right)_{\text{upper}} = \frac{1.30 \times 10^{-7}}{([r/R_{\odot}] - 1.076)^{4.73}}, \quad (17)$$

and these fits apply mainly to heights between 1.45 and $5 R_{\odot}$.

The measured stray-light data points in Figure 4 were obtained from several sources. Pre-launch laboratory testing provided the upper limit value of 10^{-8} (filled circle) at $r = 2.7 R_{\odot}$ (Kohl *et al.*, 1995). Observations of the faint Si III 1206 Å emission line – which has no coronal counterpart and is 100% stray light when measured by UVCS – were made in June 1996 (triangles) and scaled to the disk intensity of H I Ly α to obtain the stray-light suppression ratio (Gardner *et al.*, 1996). Additional data points obtained from measurements of the C III 977 Å line (squares) are also shown. Several of these measurements were discussed by Kohl *et al.* (1999). The remaining measurements are those at $1.64 R_{\odot}$ (Raymond *et al.*, 2003) and at $3.5 R_{\odot}$ (Suleiman *et al.*, 1999). In the latter two cases, only the total intensities were reported in the cited papers. These values were normalized to the solar disk and scaled to H I Ly α using the relative line intensities of Vernazza and Reeves (1978) and the time-dependent irradiance measurements of Woods *et al.* (2000). The error bars on the C III points were estimated from the assumption of an overall 50% uncertainty, which can be split up evenly between 25% uncertainties in the numerator [I_{stray}] and the denominator [I_{\odot}].

Figure 4 does not show data for distances larger than $r_{\text{obs}} \approx 4 R_{\odot}$. At these large observation heights, the measured stray light is dominated by a roughly constant background. This background is likely to be the result of several effects, including the dust-scattered F-corona, interstellar line emission (for H I Ly α and other lines of neutral species), and possibly other sources of instrumental stray light that are negligible at lower heights. In visible-light Lyot coronagraphs, a constant stray-light background of this kind is often the result of dust particles on the primary mirror (Nelson *et al.*, 2008). However, for the externally-occulted design of UVCS – in which the relatively small primary mirror is never exposed to direct sunlight – the effects of dust have been considered negligible at both visible and ultraviolet wavelengths (Romoli *et al.*, 1993; Kohl *et al.*, 1995). The vast majority of UVCS coronal measurements have been made within the range of heights shown in Figure 4.

For any given observation height, the intensity of the extended corona can vary by several orders of magnitude. Figure 4 shows the mean radial dependence of the intensity of H I Ly α in polar coronal holes measured during the 1996 – 1997 minimum of solar activity (Cranmer *et al.*, 1999). Coronal holes are the lowest-intensity structures in the extended corona, and thus they represent the most stringent requirements on stray-light suppression. The coronal intensities were normalized by dividing by a disk intensity typical for the time period of these solar-minimum observations, $I_{\odot} = 5.3 \times 10^{15}$ photons $\text{s}^{-1} \text{cm}^{-2} \text{sr}^{-1}$ (e.g., Woods *et al.*, 2000). Even the emission from coronal holes is significantly larger than the modeled and measured stray-light levels for H I Ly α . Other spectral lines tend to exhibit larger ratios of I_{cor}/I_{\odot} than H I Ly α , so the stray light is less of a contaminant.

In order to scale the above results to other spectral lines, the overall wavelength dependence of I_{stray} must be calculated. The diffraction from the external occulter depends on λ because of the definition of v in Equation (3). Also, the total rate of diffraction and scattering through the slit [Equation (7)] scales differently with λ depending on whether the non-specular stray light is dominated by finite mirror-size

diffraction or by micro-roughness. At a standard observation height of $2 R_{\odot}$, we computed I_{stray} for a range of wavelengths between half and twice that of H I Ly α . The lower-limit case of $\sigma = \omega = 0$ gives rise to an approximate wavelength dependence $I_{\text{stray}} \propto \lambda^{1.91}$. The empirical upper-limit choice of mirror parameters gives $I_{\text{stray}} \propto \lambda^{0.74}$. These exponents increase slowly as a function of increasing height. For the bright O VI 1032, 1037 Å doublet, there is only a 15% relative separation in wavelength from 1216 Å. Since the uncertainties in the model parameters exceed this level at any given height, it is reasonable to just use the modeled value of I_{stray} that was computed for H I Ly α .

7. Conclusions

The primary aim of this paper has been to construct a model of the ultraviolet stray-light properties of the UVCS instrument on SOHO. The model has essentially no freely adjustable parameters, with the possible exception of the parameters σ and ω that define the mirror imperfections. Estimates of these parameters were obtained from pre-launch laboratory tests and in-flight measurements. A completely separate set of existing measurements of the stray-light suppression ratio for H I Ly α was used to test the model. As can be seen in Figure 4, the modeled stray light agrees well with these measurements.

It is interesting to investigate how much of an improvement in stray-light suppression can be made by various changes to the externally occulted coronagraph design exemplified by UVCS. Equation (7) indicates that even if the mirror were made to be perfectly smooth ($\sigma = 0$) and ideally diffraction-limited ($W = 1$, $D_x = \Lambda$), there would still be a finite level of non-specular stray light due to diffraction by the finite-sized mirror. Reductions in the amount of non-specular radiation can then be achieved by increasing the mirror size [D_x] or by increasing the magnitudes of the non-specular angles [θ_x] that pass through the slit.

Designs for next-generation coronagraph spectrometers have also achieved improvements in performance by increasing the distance [H_{exo}] between the mirror and external occulter (Kohl *et al.*, 2006; Kohl *et al.*, 2008). An increase in H_{exo} results in a smaller value of H_{diff} [Equation (2)], which leads to smaller non-specular angles [θ_x]. Taken by itself, this would give rise to an increase in the non-specular intensity that scatters and diffracts from the mirror into the slit. However, this effect is more than offset by the larger unvignetted mirror area that becomes available when H_{exo} is increased (*i.e.*, an increase in x_2). The larger mirror area gives rise to a “deeper shadow” under the external occulter, which is equivalent to a larger extent of v in Figure 2. This results in a lower overall amount of diffracted light striking the mirror. Also, the larger available mirror area allows more coronal rays to be collected, thus increasing the overall instrumental sensitivity. These advantages, together with improvements in mirror reflectivity and detector efficiency, can give rise to several orders of magnitude improvement in sensitivity compared to UVCS/SOHO.

Appendix

A. Derivation of Non-Specular Intensity Profiles

Here we describe the angular dependence of non-specular diffraction and scattering that arise from reflection (at nearly normal incidence) from a mirror of finite size and with a non-ideal surface. The fraction of the incident intensity I_0 scattered into a differential solid angle $[d\Omega]$ is defined here as

$$S(\mathbf{q}) = \frac{dI}{I_0 d\Omega}, \quad (18)$$

where the scattering wavevector \mathbf{q} is the vector difference between the incoming and reflected photon wavevectors \mathbf{k} . Thus, if the mirror surface is assumed to lie in the x, y plane, then $(q_x, q_y, q_z) \approx 2\pi(\theta_x, \theta_y, 2)/\lambda$. The goal of this Appendix is to show how S depends explicitly on the non-specular angles θ_x and θ_y . The specularly reflected ray is defined as $\theta_x = \theta_y = 0$.

In the optics literature, the differential scattering fraction defined above is often described using other terms. A frequently used variant is the bi-directional reflectance distribution function (BRDF), which is defined as

$$\text{BRDF} = \frac{1}{\cos \Theta} \frac{dI}{I_0 d\Omega}, \quad (19)$$

and where Θ is the scattering angle measured from the local normal to the mirror surface (Bennett and Mattsson, 1999). Another commonly used term is the power spectral density (PSD), which is a measure of the angular distribution of fluctuations on the mirror surface itself. The PSD can be expressed in similar units as the angular distribution of reflected power, and

$$\text{PSD} = \frac{\lambda^4}{16\pi^2 \mathcal{R}} \frac{dI}{I_0 d\Omega}. \quad (20)$$

The dimensionless quantity \mathcal{R} is the overall reflectivity of the mirror, and it is often called an ‘‘optical factor’’ that depends on wavelength, the angles of incidence and reflection, and the degree of polarization of the incident and reflected beams (Bennett, 2003). In order to separate out the problem of mirror reflectivity from the problems of non-specular scattering and diffraction, the analysis below makes the assumption that $\mathcal{R} = 1$.

The angular intensity profile can be derived by applying the Born approximation from scattering theory (*e.g.*, Sinha *et al.*, 1988; Church and Takacs, 1993; Gullikson *et al.*, 1997). If the reflectivity of the mirror is assumed to be perfect, the Born approximation can be expressed as

$$S(\mathbf{q}) = \frac{1}{A\lambda^2} \int dx dy \int dx' dy' e^{-i\mathbf{q}\cdot(\mathbf{r}-\mathbf{r}')}. \quad (21)$$

Both sets of spatial integrals are taken over the mirror area A in the x, y plane. The position vector \mathbf{r} depends not only on the horizontal position, but also on the spatially varying mirror height $z(x, y)$.

In the UVCS instrument, the most important orientation for the non-specular diffraction and scattering is the θ_x direction (*i.e.*, the left–right horizontal direction in Figures 1 and 3). Because light from a given point in the y -direction (on the sky or on the external occulter) fills the mirror in the y -direction, there ends up being a wide range of θ_y scattering angles that go through the slit. Thus, we first solve Equation (21) and then integrate over all θ_y angles to obtain the differential scattering rate $dI/(I_0 d\theta_x)$. Sections A.1 and A.2 give independent calculations of this quantity in two limiting regimes of the spatial scales of mirror imperfections. Equation (7) above estimates their combined effect as the sum of the two rates.

A.1. Non-Specular Scattering due to Micro-Roughness

When only small-scale statistical fluctuations in the mirror surface are taken into account, it is possible to describe the mirror height with spatially averaged moments. The mean height is defined as

$$\langle z \rangle = \frac{1}{A} \int dx dy z(x, y) = 0 , \quad (22)$$

and the r.m.s. surface roughness is given by $\langle z^2 \rangle^{1/2} = \sigma$. As defined here, σ contains no information about the horizontal distribution of microscopic structures on the mirror surface. Typically, laboratory measurements of σ are dependent on the range of horizontal scales that were probed. Many real surfaces have a “fractal” distribution of surface fluctuations that are ill-described by a single σ . To begin the process of characterizing the horizontal scales, though, we define an autocorrelation function

$$C(s, t) = \frac{1}{A} \int dx dy z(x, y) z(x - s, y - t) \quad (23)$$

and we assume the surface is isotropic on small enough scales such that C is a function of only $r \equiv (s^2 + t^2)^{1/2}$.

With the above definitions, the scattering integrals in Equation (21) can be shown to reduce to

$$S(\theta) = \frac{2\pi}{\lambda^2} \int dr r \exp \left\{ -\frac{16\pi^2}{\lambda^2} [\sigma^2 - C(r)] \right\} J_0 \left(\frac{2\pi r \theta}{\lambda} \right) \quad (24)$$

where J_0 is the zeroth-order Bessel function of the first kind, and $\theta = (\theta_x^2 + \theta_y^2)^{1/2}$ is the full magnitude of the scattering angle away from the specular beam. In this section we assume the integration over r can be taken from zero to infinity, which ignores the finite size of the mirror. This is equivalent to assuming that the patterns of micro-roughness are small in comparison to the mirror size. We can make use of a commonly used (and empirically derived) parameterization for the autocorrelation function,

$$C(r) = \sigma^2 \exp [-(2\pi r/\Lambda)^{2h}] , \quad (25)$$

in which Λ is a horizontal correlation wavelength (or coherence length scale) for the mirror and h is a texture parameter that describes the shapes of the surface features.

Small values ($h \ll 1$) indicate extremely jagged surfaces and large values ($h \approx 1$) describe smooth crests and troughs. Sometimes the autocorrelation function is expressed as a sum of several terms each similar in form to Equation (25), but with different values of h (Elson *et al.*, 1993). In that case, the r.m.s. surface roughness σ in each term can refer to different ranges of spatial scale. The special value $h = 1/2$ is often identified as a “conventional surface finish,” and we will restrict ourselves to this value for simplicity (see Sinha *et al.*, 1988; Church and Takacs, 1993; Fineschi *et al.*, 1994). Using this value, combined with the approximation of small-scale surface roughness ($\sigma \ll \lambda$), the intensity scattering profile becomes

$$S(\theta) = \frac{\delta(\theta)}{2\pi\theta} + \frac{8\pi\sigma^2\Lambda^2}{\lambda^4[1 + (\theta\Lambda/\lambda)^2]^{3/2}}. \quad (26)$$

The first term, proportional to a Dirac delta function, describes the ideal specular beam. The second term is the scattering due to micro-roughness, and its integral over all solid angles gives the so-called total integrated scatter (TIS), or

$$\text{TIS} = 2\pi \int_{\theta \neq 0} d\theta S(\theta) = \frac{16\pi^2\sigma^2}{\lambda^2}. \quad (27)$$

Noting that $\theta^2 = \theta_x^2 + \theta_y^2$, we assume $\theta_x \neq 0$ and integrate over θ_y to obtain

$$\frac{dI}{I_0 d\theta_x} = \frac{16\pi\sigma^2\Lambda}{\lambda^3[1 + (\theta_x\Lambda/\lambda)^2]}. \quad (28)$$

For large angles, far from the specular beam (*i.e.*, $\theta_x \gg \lambda/\Lambda$) this reduces to

$$\frac{dI}{I_0 d\theta_x} \approx \frac{16\pi\sigma^2}{\lambda\Lambda\theta_x^2}, \quad (29)$$

which is used in Equation (7) above.

A.2. Non-Specular Diffraction due to Finite Mirror Size and Aberrations

For an illuminated mirror that reflects a finite-sized (rectangular) incident beam of light, diffraction will broaden the reflected beam and give rise to power at non-specular angles. This situation is similar to the diffraction of parallel rays that pass through a rectangular aperture (see, *e.g.*, Schroeder, 2000; Hecht, 2002).

The simplest case of a mirror with an ideal surface can be treated by assuming $z = 0$ in Equation (21) and taking the integration limits to be finite in both x and y . This yields

$$S(\theta_x, \theta_y) = \frac{D_x D_y}{\lambda^2} \left(\frac{\sin u_x}{u_x} \right)^2 \left(\frac{\sin u_y}{u_y} \right)^2 \quad (30)$$

where $D_x = (x_{\max} - x_{\min})$ and $D_y = (y_{\max} - y_{\min})$ are the dimensions of the illuminated part of the mirror. The dimensionless angle coordinates are defined as $u_i = \pi D_i \theta_i / \lambda$, for $i = x, y$. Equation (30) is the well-known diffraction pattern that drops

off as u^{-2} along the normal axes of the rectangular aperture, and as u^{-4} along the diagonals. As above, we integrate over θ_y to obtain

$$\frac{dI}{I_0 d\theta_x} = \frac{D_x}{\lambda} \left(\frac{\sin u_x}{u_x} \right)^2 \approx \frac{\lambda}{2\pi^2 D_x \theta_x^2} . \quad (31)$$

The latter approximation above is taken in the limiting case of large-angle scattering ($u_x \gg 1$), where the mean behavior of the function $(\sin u/u)^2$ can be approximated as $1/(2u^2)$.

For diffraction off a mirror containing large-scale aberrations, we must again apply a variable mirror height $z(x, y)$ in Equation (21). This is traditionally done by inserting a phase factor that takes account of the optical-path differences between the aberrated wavefronts and the ideal, non-aberrated wavefronts. Born and Wolf (1999) and Schroeder (2000) defined these phase factors in terms of Zernike polynomials for various types of common mirror deformation patterns. Aberrations change the diffraction profile defined above in two distinct ways:

- i) They enhance the non-specular scattering in the far wings of the profile (see, *e.g.*, Figures 10.12 to 10.17 of Schroeder, 2000). Here, we take this into account by multiplying Equation (31) by a wing enhancement factor W .
- ii) They broaden the specular beam, which for a finite mirror or aperture is defined according to how far from the ideal specular ray one must go to encompass a specified level of “encircled energy.” The broadening of the specular beam is related closely to how far the actual mirror is from the diffraction limit.

In order to quantify these effects, we calculated a range of diffraction profiles for various types of aberration. Kohl *et al.* (1995) noted that spherical aberrations tended to be the dominant type for the UVCS mirrors. The remainder of this section concentrates only on that type. The standard measure of the magnitude of an aberration is the r.m.s. wavefront error ω , which is usually expressed as a dimensionless number of wavelengths ω/λ . The relative departures from the perfect (non-aberrated) case were computed for a circular mirror, but they should be comparable for mirrors of other shapes.

Figure 5 shows both the broadening of the specular beam and the enhancement of the power-law scattering wing as a function of the wavefront error. The width of the specular beam was computed by determining the angular radius $[\theta_s]$ at which the encircled energy was 0.838 times the total energy distributed over all angles. This fraction is equivalent to the light enclosed by the the classical “Airy disk” (see Hecht, 2002). For a diffraction-limited circular mirror without aberrations, $\theta_s = 1.22\lambda/D$. A mirror with aberrations has a larger value of θ_s and thus corresponds to a smaller effective diameter D_{eff} , which would have given rise a specular beam of identical width in the absence of aberrations. Once θ_s has been computed for a given magnitude of the spherical aberration, it is then possible to solve for the ratio

$$\frac{D}{D_{\text{eff}}} \approx \frac{\theta_s}{1.22 \lambda/D} \geq 1 . \quad (32)$$

The quantity D_{eff} characterizes the horizontal spatial scales of large wavefront deviations on the mirror surface, just as Λ characterizes the coherence length of the micro-scale wavefront deviations. Interestingly, laboratory and in-flight measurements

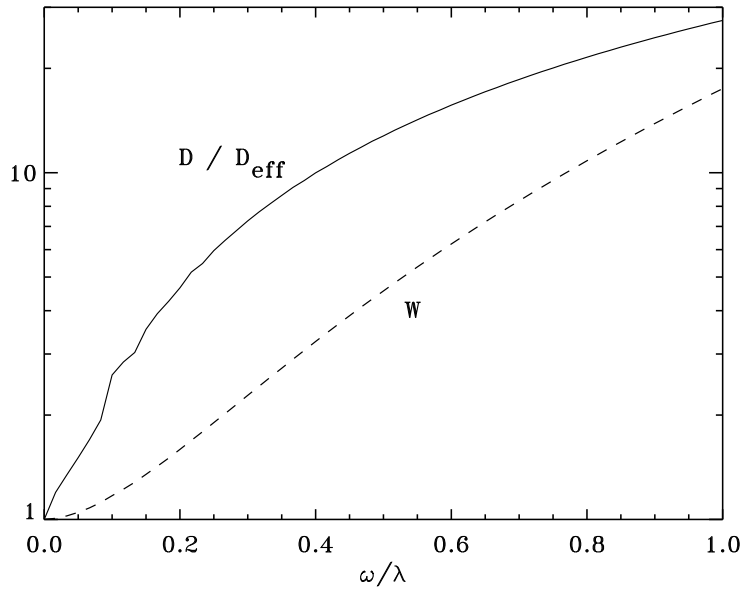


Figure 5. Effects of spherical aberrations on the ratio of the mirror diameter D to the effective diameter D_{eff} (solid curve) and on the relative wing enhancement W (dashed curve).

for the UVCS Ly α primary mirror yielded similar values for the ratios D_x/D_{eff} and D_x/Λ (see Section 6).

We computed the magnitude of the enhanced diffraction wing by fitting the angular dependence of $S(\theta)$ with a power-law (outside the specular beam). The ratio W was found by taking the ratio of the numerically computed wing intensity to that produced by a mirror with no aberrations. The dependence of this ratio is also shown in Figure 5. Thus, if any one of the three quantities (ω/λ , D/D_{eff} , or W) is specified for a given mirror, Figure 5 can be used to estimate the other two.

Acknowledgements This work has been supported by the National Aeronautics and Space Administration (NASA) under grants NNX07AL72G, NNX08AQ96G, NNX09AB27G, and NNX09AN61G to the Smithsonian Astrophysical Observatory, by Agenzia Spaziale Italiana, and by the Swiss contribution to the ESA PRODEX program. SOHO is a project of international cooperation between NASA and the European Space Agency (ESA).

References

- Abramowitz, M., Stegun, I.A.: 1972, *Handbook of Mathematical Functions*, Dover Publications, New York, p. 300.
- Bennett, J.M.: 2003, in Driggers, R.G. (ed.), *Encyclopedia of Optical Engineering*, Marcel Dekker, New York, 2746.
- Bennett, J.M., Mattsson, L.: 1999, *Introduction of Surface Roughness and Scattering*, 2nd ed., Optical Society of America, Washington, DC.
- Billings, D.E.: 1966, *A Guide to the Solar Corona*, Academic Press, New York.
- Born, M., Wolf, E.: 1999, *Principles of Optics: Electromagnetic Theory of Propagation, Interference and Diffraction of Light*, 7th ed., Cambridge University Press, Cambridge, UK.

- Church, E.L., Takacs, P.Z.: 1993, *App. Opt.* **32**, 3344.
- Cranmer, S.R.: 2009, *Living Rev. Solar Phys.* **6**, No. 3, <http://solarphysics.livingreviews.org/Articles/lrsp-2009-3>. ■
- Cranmer, S.R., Kohl, J.L., Noci, G., Antonucci, E., Tondello, G., Huber, M.C.E., Strachan, L., Panasyuk, A.V., Gardner, L.D., Romoli, M., et al.: 1999, *Astrophys. J.* **511**, 481.
- Curdt, W., Tian, H., Teriaca, L., Schühle, U., Lemaire, P.: 2008, *Astron. Astrophys.* **492**, L9.
- Domingo, V., Fleck, B., Poland, A.I.: 1995, *Solar Phys.* **162**, 1.
- Elson, J.M., Bennett, J.M., Stover, J.C.: 1993, *App. Opt.* **32**, 3362.
- Evans, J.W.: 1948, *J. Opt. Soc. Am.* **38**, 1083.
- Fineschi, S., Romoli, M., Hoover, R.B., Baker, P.C., Zukic, M., Kim, J., Walker, A.B.: 1994, *Proc. SPIE* **2100**, 78.
- Fleck, B., Švestka, Z. (eds.): 1997 *The First Results from SOHO*, Kluwer, Dordrecht, The Netherlands.
- Gardner, L.D., Kohl, J.L., Daigneau, P.S., Dennis, E.F., Fineschi, S., Michels, J., Nystrom, G.U., Panasyuk, A., Raymond, J.C., Reisenfeld, D.J., et al.: 1996, *Proc. SPIE* **2831**, 2.
- Gullikson, E.M., Stearns, D.G., Gaines, D.P., Underwood, J.H.: 1997, *Proc. SPIE* **3113**, 412.
- Hecht, E.: 2002, *Optics*, 4th ed., Addison-Wesley, San Francisco.
- Howard, R.A., Moses, J.D., Vourlidis, A., Newmark, J.S., Socker, D.G., Plunkett, S.P., Korendyke, C.M., Cook, J.W., Hurley, A., Davila, J.M., et al.: 2008, *Space Sci. Rev.* **136**, 67.
- Kohl, J.L., Esser, R., Cranmer, S.R., Fineschi, S., Gardner, L.D., Panasyuk, A.V., Strachan, L., Suleiman, R.M., Frazin, R., Noci, G.: 1999, *Astrophys. J.* **510**, L59.
- Kohl, J.L., Esser, R., Gardner, L.D., Habbal, S., Daigneau, P.S., Dennis, E.F., Nystrom, G.U., Panasyuk, A., Raymond, J.C., Smith, P.L., et al.: 1995, *Solar Phys.* **162**, 313.
- Kohl, J.L., Jain, R., Cranmer, S.R., Gardner, L.D., Pradhan, A.K., Raymond, J.C., Strachan, L.: 2008, *J. Astrophys. Astron.* **29**, 321.
- Kohl, J.L., Noci, G., Antonucci, E., Tondello, G., Huber, M.C.E., Gardner, L.D., Nicolosi, P., Strachan, L., Fineschi, S., Raymond, J.C., et al.: 1997, *Solar Phys.* **175**, 613.
- Kohl, J.L., Noci, G., Cranmer, S.R., Raymond, J. C.: 2006, *Astron. Astrophys. Rev.* **13**, 31.
- Kohl, J.L., Reeves, E.M., Kirkham, B.: 1978, in van der Hucht, K., Vaiana, G. (eds.), *New Instrumentation for Space Astronomy*, Pergamon, New York, 91.
- Kohl, J.L., Weiser, H., Withbroe, G.L., Noyes, R.W., Parkinson, W.H., Reeves, E.M., Munro, R.H., MacQueen, R.M.: 1980, *Astrophys. J.* **241**, L117.
- Koutchmy, S.: 1988, *Space Sci. Rev.* **47**, 95.
- Koutchmy, S., Belmahdi, M.: 1987, *J. Optics* **18**, 265.
- Leviton, D.B., Saha, T.T., Gardner, L.D.: 1998, *Proc. SPIE* **3443**, 19.
- Nelson, P.G., Tomczyk, S., Elmore, D.F., Kolinski, D.J.: 2008, *Proc. SPIE* **7012**, 701231.
- Newkirk, G. Jr.: 1967, *Ann. Rev. Astron. Astrophys.* **5**, 213.
- Newkirk, G. Jr., Bohlin, D.: 1963, *App. Opt.* **2**, 131.
- Raymond, J.C., Ciaravella, A., Dobrzycka, D., Strachan, L., Ko, Y.-K., Uzzo, M., Raouafi, N.-E.: 2003, *Astrophys. J.* **597**, 1106.
- Romoli, M., Weiser, H., Gardner, L.D., Kohl, J.L.: 1993, *App. Opt.* **32**, 3559.
- Saha, T.T., Leviton, D.B., Glenn, P.: 1996, *App. Opt.* **35**, 1742.
- Schroeder, D.J.: 2000, *Astronomical Optics*, 2nd ed., Academic Press, San Diego.
- Sinha, S.K., Sirota, E.B., Garoff, S., Stanley, H.B.: 1988, *Phys. Rev. B.* **38**, 2297.
- Suleiman, R.M., Kohl, J.L., Panasyuk, A.V., Ciaravella, A., Cranmer, S.R., Gardner, L.D., Frazin, R., Hauck, R., Smith, P.L., Noci, G.: 1999, *Space Sci. Rev.* **87**, 327.
- Vernazza, J.E., Reeves, E.M.: 1978, *Astrophys. J. Suppl.* **37**, 485.
- Verroi, E., Frassetto, F., Naletto, G.: 2008, *J. Opt. Soc. Am. A* **25**, 182.
- Withbroe, G.L., Kohl, J.L., Weiser, H., Munro, R.H.: 1982, *Space Sci. Rev.* **33**, 17.
- Woods, T.N., Tobiska, W.K., Rottman, G.J., Worden, J.R.: 2000, *J. Geophys. Res.* **105**, 27195.

